Structural insights into electric field induced polarization and strain responses in $K_{0.5}Na_{0.5}NbO_3$ modified morphotropic phase boundary compositions of $Na_{0.5}Bi_{0.5}TiO_3$-based lead-free piezoelectrics

Gobinda Das Adhikary,[1] Gudeta Jafo Muleta,[1] Getaw Abebe Tina,[1] Deepak Sharma,[1] Bhoopesh Mahale,[1]
Lucas Lemos da Silva [ORCID],[2,3] Manuel Hinterstein,[2,3] Anatoliy Senyshyn,[4] and Rajeev Ranjan [ORCID][1,*]

[1]*Department of Materials Engineering, Indian Institute of Science, Bangalore 560012, India*
[2]*Fraunhofer IWM, 79108 Freiburg, Germany*
[3]*Institute for Applied Materials, Karlsruhe Institute of Technology, 76131 Karlsruhe, Germany*
[4]*Forschungsneutronenquelle Heinz Maier-Leibnitz (FRM II), Technische Universität München,
Lichtenbergstrasse 1, D-85747 Garching b. München, Germany*

$K_{0.5}Na_{0.5}NbO_3$ (KNN)-modified morphotropic phase boundary (MPB) compositions of the two $Na_{0.5}Bi_{0.5}TiO_3$-based lead-free piezoelectrics, namely, $0.94Na_{0.5}Bi_{0.5}TiO_3$-$0.06BaTiO_3$ (NBT-6BT) and $0.80Na_{0.5}Bi_{0.5}TiO_3$-$0.20K_{0.5}Bi_{0.5}TiO_3$ (NBT-20KBT) are model systems exhibiting large ($>0.4\%$) electric-field-driven strain. There is a general perception that (i) increasing KNN concentration monotonically weakens the direct piezoelectric response (d_{33}), and (ii) maximum electrostrain occurs when KNN pushes the system in the fully ergodic relaxor state. We have examined these issues using various complementary techniques involving electrostrain, piezoelectric coefficient (d_{33}), ferroelectric switching-current measurements, and field-driven structural studies on the global and local scales using laboratory and synchrotron x-ray diffraction, neutron powder diffraction, and Eu^{+3} photoluminescence techniques. Our investigations revealed the following important features: (i) In the low-concentration regime, KNN induces a tetragonal ferroelectric distortion, which improves the weak signal piezoresponse. (ii) Beyond a threshold concentration, in-phase octahedral tilt sets in and weakens the long-range ferroelectric order to partially stabilize an ergodic state. (iii) The maximum electrostrain ($\sim0.6\%$) is achieved in the mixed (nonergodic + ergodic) state. (iv) The mixed state invariably exhibits a less-known phenomenon of field-driven ferroelectric-to-relaxor transformation during bipolar field cycling. (v) The enhanced electrostrain in the mixed state is associated with the electric field increasing the correlation lengths of the short-ranged tetragonal and rhombohedral ferroelectric regions without overall transformation of one phase to the other. We summarize the findings of this work in a comprehensive electric field composition (E-x) phase diagram. The findings reported here are likely to be true for other NBT-based MPB systems.

I. INTRODUCTION

For over a decade and a half, increased environmental and health concerns associated with the toxicity of Pb in commercial lead-zirconate-titanate–based piezoelectric materials have motivated the scientific community to explore Pb-free alternatives [1–8]. The emphasis has been to improve the electromechanical responses of the few Pb-free ferroelectric compounds available in the oxide perovskite family like $BaTiO_3$ (BT), $(K, Na)NbO_3$, $K_{0.5}Bi_{0.5}TiO_3$ (KBT), $Na_{0.5}Bi_{0.5}TiO_3$ (NBT), and $BiFeO_3$ by chemical modifications. While over the years these efforts have led to a remarkable improvement in the direct piezoelectric coefficients (d_{33}) of BT-based [9–16] and $K_{0.5}Na_{0.5}NbO_3$ (KNN)-based systems [17–19] (d_{33}) ~ 500–$600\,pC/N$), there has been no similar progress in improving d_{33} of the NBT- and KBT-based systems. The maximum d_{33} of NBT-based systems is $\sim200\,pC/N$ [7,20]. However, the discovery of a relatively

high unipolar electrostrain ($>0.4\%$) in the KNN-modified compositions of the morphotropic phase boundary (MPB) system $0.94Na_{0.5}Bi_{0.5}TiO_3$-$0.06BaTiO_3$ [21] has given NBT-based piezoelectrics a unique identity as large-strain actuator materials.

NBT belongs to the family of relaxor ferroelectrics [20,22–24]. Although it exhibits a long-range rhombohedral ferroelectric structural distortion [25], the relaxor ferroelectric behavior is caused by the inherent tendency of the system to develop structural disorder caused by the local displacement of Na/Bi which is incompatible with the average rhombohedral symmetry [26]. The displacement disorder is also found on the oxygen sublattice due to presence of $a^0a^0c^+$-tilted octahedral regions on the nanoscale [27]. Following Jones and Thomas [28], the $a^0a^0c^+$-tilted octahedral region is generally referred to as the $P4bm$ phase. The interaction of the short-ranged $a^0a^0c^+$ regions with the relatively long-ranged $a^-a^-a^-$-tilted rhombohedral regions [29] makes the average structure appear as monoclinic (Cc) [30,31]. The nano-sized $a^0a^0c^+$-tilted regions observed at room temperature in NBT are considered the residue of the high-temperature

nonferroelectric tetragonal ($P4/mbm$) phase [32] and can be suppressed by the application of a strong electric field [33–35]. On the global scale, this manifests as a field-driven irreversible Cc-to-rhombohedral ($R3c$) transformation [33,34]. The two important solid solutions of NBT which have attracted considerable attention over the years are the ones with the tetragonal ($P4mm$) ferroelectric perovskites such as KBT and BT. Both (1-x)NBT-(x)KBT and (1-y)NBT-(y)BT exhibit MPBs at $x = 0.20$ [36–38] and $y = 0.06$ [35,39,40], respectively, at which the piezoelectric coefficient (d_{33}) is maximum. In a recent study, Adhikary *et al.* [41] have shown that, in addition to the interferroelectric $R3c$-$P4mm$ structural instability, the MPB in NBT-based piezoelectrics is also characterized by the ordered-$P4bm$ and disordered-$P4bm$ boundaries. One of the peculiar features of the NBT-based MPB systems is the anomalous decrease in the depolarization temperature as the MPB composition is approached [42,43].

Ever since the discovery of unipolar electrostrain >0.4% in KNN-modified MPB composition of the NBT-BT [(0.94-y)NBT-0.06BT-yKNN] by Zhang *et al.* [21], there has been continuous effort to increase the electrostrain level in other derivatives of NBT-based piezoelectrics. A similar level of electrostrain has been reported in KNN-modified NBT-KBT [(0.80-x)NBT-0.20KBT-xKNN] [44–47] and other modifications like SrTiO$_3$ [48], LiNbO$_3$ [49], and BiAlO$_3$ [50]. The large electrostrain in different derivatives of NBT-BT/NBT-KBT has been variously explained as field-driven antiferroelectric-to-ferroelectric transformation [51], reversible field-driven nonpolar (ergodic)-to-ferroelectric transformation [52,53], a combination of electrostrictive and converse piezoelectric effects [46], large reversible switching of tetragonal domains [54], breaking of the Bi-O hybridization [55], etc. For the KNN-modified MPB compositions of NBT-BT and NBT-KBT, it is generally reported that KNN monotonically weakens the piezoelectric response (d_{33}) [21,56,57]. Further, some studies reported that the large electrostrain in KNN-modified NBT-BT occurs when the system is entirely in the ergodic relaxor (ER) state [45,52,53]. The relaxor state has generally been attributed to the $P4bm$ phase and the ferroelectric state to the $R3c$ phase [58,59]. Given that the critical compositions of NBT-KBT and NBT-BT also represent a $R3c$-$P4mm$ interferroelectric instability [41,60,61], the possibility of stabilizing ferroelectric $P4mm$ distortion cannot be ruled out. For a better appreciation of the mechanism governing strain enhancement in KNN-modified MPB compositions of NBT-BT and NBT-KBT, it is important to understand the subtlety of the structural states and how they evolve with composition and electric field. In this paper, we have attempted to resolve this issue using a series of structural and physical property measurements on KNN-modified MPB compositions 0.80NBT-0.20KBT (NBT-20KBT) and 0.94NBT-0.06BT (NBT-6BT). While we prove that the large electrostrain occurs when the system happens to be in the ergodic + nonergodic mixed states and not in the fully ergodic state, we employed a series of complementary tools to probe the nature of structural changes, both on the local and global scales, accompanying the strain enhancement. The structure on the global scale was investigated using a combination of laboratory x-ray, synchrotron x-ray, and neutron diffraction techniques. The average structural information on the local

scale was inferred using an Eu^{+3} photoluminescence (PL) technique [38,61–64]. We also found that, in the presence of the ER state, the field-stabilized long-range ferroelectric order can transform to a nonergodic relaxor (NER) state during field reversal.

II. EXPERIMENTAL

KNN-modified MPB compositions of NBT-BT and NBT-KBT were synthesized as per the chemical formulas (0.80-x)NBT-0.20KBT-(x)KNN [NBT-20KBT-xKNN] and (0.94-y)NBT-0.06BT-yKNN [NBT-6BT-yKNN] using the conventional solid-state reaction method [42]. Electrical properties were measured on pellets of an average density ∼95%. The sintered pellets with diameters of 10–12 mm and thickness of ∼0.4 mm were painted with high-temperature silver paste for electrical contact and were poled by applying a dc field of 60 kV/cm for 20 min. The direct longitudinal piezoelectric coefficient (d_{33}) of the poled pellet was measured using Piezotest, PM300 with applied force 0.25 N and frequency 110 Hz. A Precision Premier II tester (Radiant Technologies, Inc.) was used to obtain the polarization–electric field (P-E) hysteresis measurements and current density (J) vs electric field measurements at 1 Hz. Electrostrain vs electric field (S-E) measurement was carried out using an MTI-2100 photonic sensor attached to the Radiant setup. Thermal depoling current measurements were carried out using an Electrometer (Keithley, 6514) by heating poled pellets at 3 °C/min. Eu^{+3} PL spectra were collected from poled and unpoled pellets using a 532-nm laser attached to a LabRAM HR (HORIBA) spectrometer. Dielectric measurements were carried out with a Novocontrol Alpha-A impedance analyzer. Neutron powder diffraction (NPD) data were collected at SPODI, FRM-II, Germany (wavelength of 1.54815 Å) [65]. X-ray powder diffraction (XRPD) studies were carried out with a Rigaku Smartlab x-ray diffractometer with monochromatic Cu $K\alpha_1$ radiation in reflection geometry. The diffractometer is equipped with a Johansson monochromator in the incident beam, which results in pure Cu-$K\alpha_1$ radiation. For comparison, we also carried out x-ray diffraction (XRD) measurements on dense pellet specimens in the transmission geometry using high-energy synchrotron x rays (wavelength 0.207308 Å) at the P02.1 diffractometer at Petra, DESY. XRPD patterns of the unpoled specimens were collected after annealing the powder at 700 °C for 2 h and obtained after crushing the sintered pellets to remove the effect of residual stress incurred during the grinding process. XRPD patterns of the poled specimens were obtained after crushing the poled pellets to powder. Structural analysis was carried out using the FULLPROF package [66].

III. RESULTS

A. Physical properties

Figures 1(a) and 1(b) show the longitudinal weak-signal piezoelectric coefficient (d_{33}) as a function of composition for NBT-20KBT-xKNN and NBT-6BT-yKNN, respectively. For the NBT-20KBT-xKNN series, d_{33} improves from 160 pC/N for $x = 0.00$ to ∼210 pC/N for $x = 0.015$. Following the same trend, d_{33} improves from 150 to 200 pC/N on increasing
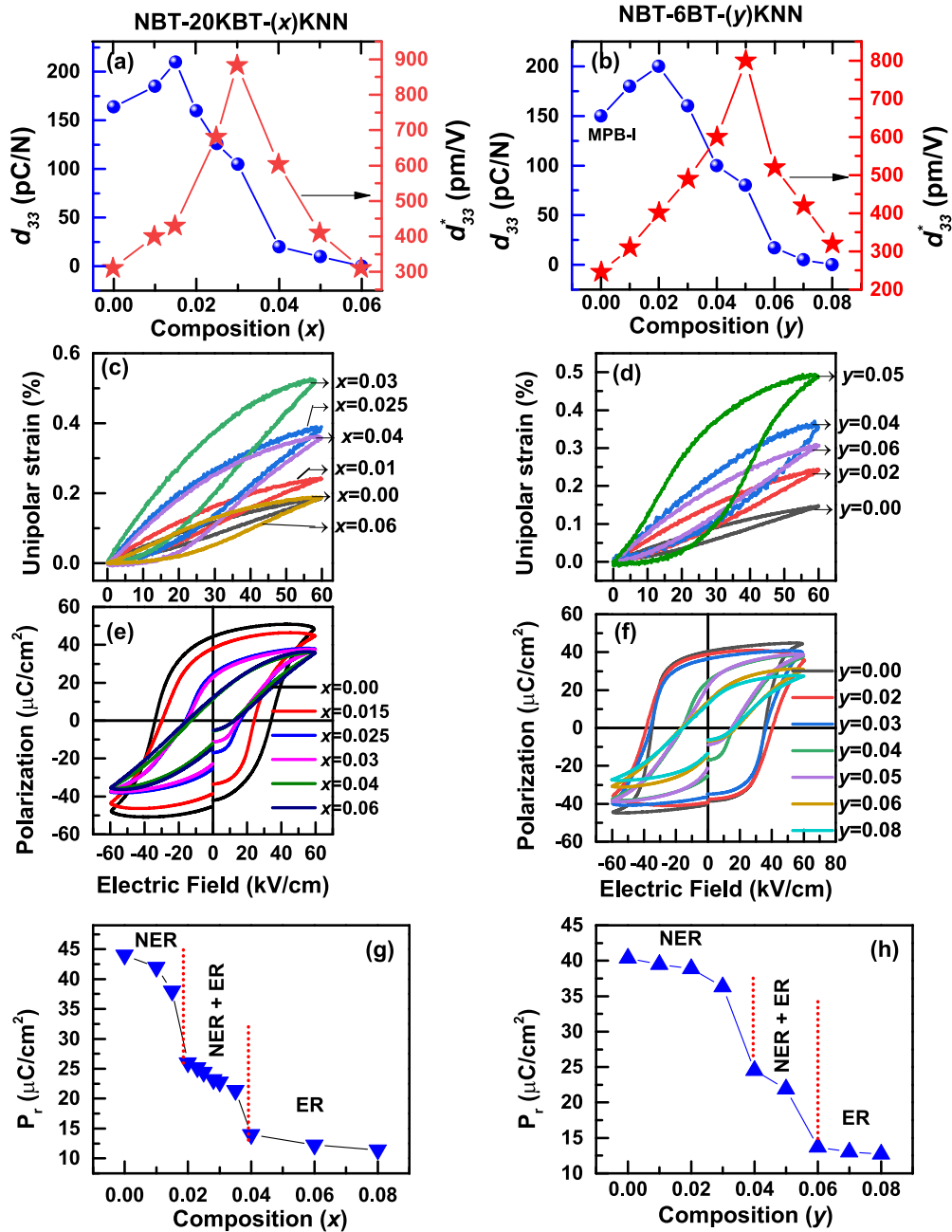
FIG. 1. Composition dependence of the piezoelectric coefficient (d_{33}) of (a) $(0.80\text{-}x)\text{Na}_{0.5}\text{Bi}_{0.5}\text{TiO}_3\text{-}0.20\text{K}_{0.5}\text{Bi}_{0.5}\text{TiO}_3\text{-}x\text{K}_{0.5}\text{Na}_{0.5}\text{NbO}_3$ [NBT-20KBT-xKNN] and (b) $(0.94\text{-}y)\text{Na}_{0.5}\text{Bi}_{0.5}\text{TiO}_3\text{-}0.06\text{BaTiO}_3\text{-}y\text{K}_{0.5}\text{Na}_{0.5}\text{NbO}_3$ [NBT-6BT-yKNN]. (c) and (d) Unipolar strain and (e) and (f) polarization-electric field (P-E) hysteresis loops for different compositions. (g) and (h) Composition dependence of the remanent polarization of NBT-20KBT-xKNN and (h) NBT-6BT-yKNN, respectively.

the KNN concentration to $y = 0.02$ for the NBT-6BT-yKNN series [Fig. 1(b)]. Beyond these critical compositions, d_{33} decreases monotonically. The composition $x = 0.03$, on the other hand, shows the maximum electrostrain values ($\sim 0.62\%$ bipolar and 0.55% unipolar at 60 kV/cm) for NBT-20KBT-xKNN (Figs. 1(c) and S1(a) in the Supplemental Material [67]). NBT-6BT-yKNN exhibits maximum electrostrain at $y = 0.05$ (bipolar 0.53% and unipolar 0.5%, Figs. 1(d) and S1(b) in the Supplemental Material [67]). The depolarization temperature (T_d), measured from the peak in the depoling current vs the temperature of poled pellets (Fig. S2(a) in the Supplemental Material [67]), suggests that T_d decreases monotonically with increasing x, Fig. S2(b) in the Supplemental Material [67]. For $x = 0.03$, the composition exhibiting maximum electrostrain is $T_d \sim 60\,^{\circ}\text{C}$. This, together with the fact that d_{33} of this composition is still ~ 105 pC/N [Fig. 1(a)], confirms that the composition exhibiting the maximum electrostrain in the series is not fully in the ER state but also has field-stabilized long-range ferroelectric order. An important point to note is that the remanent polarization (P_r) shows abrupt decreases at two compositions, namely, $x = 0.02$ and 0.04 for NBT-20KBT-xKNN [Figs. 1(e) and 1(g)] and at
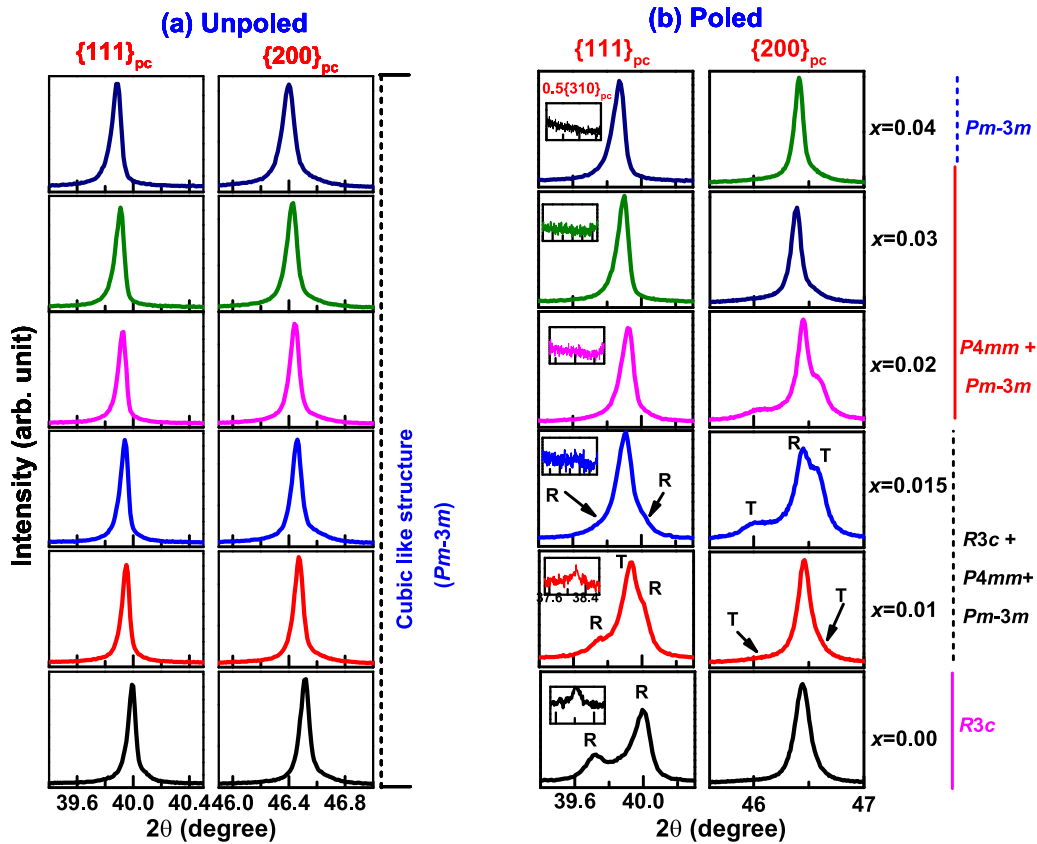
FIG. 2. X-ray powder diffraction Bragg profiles of pseudocubic $\{111\}_{pc}$ and $\{200\}_{pc}$ of (a) unpoled and (b) poled NBT-20KBT-xKNN for different KNN concentration.

$y = 0.04$ and 0.06 for NBT-6BT-yKNN [Figs. 1(f) and 1(h)]. A careful observation suggests that these abrupt drops are due to a qualitative change in the shape of the *P-E* loops, the details of which can be found in Sec. III G.

B. Average global structure: XRD

Figures 2 and 3 show the composition evolution of the x-ray Bragg profiles of $\{111\}_{pc}$ and $\{200\}_{pc}$ pseudocubic reflections of NBT-20KBT-xKNN and NBT-6BT-yKNN, respectively, in their unpoled and poled states. Following our previous strategy [42,63,68,69], the diffraction patterns of the poled specimens were collected after grinding poled pellets to powder. The powdered poled pellet yields a preferred orientation-free diffraction pattern while retaining the irreversible structural changes brought about by the poling field. For systems in the NER ferroelectric state, poling stabilizes a long-range ferroelectric order, the structure of which can be determined by examining the nature of splitting of the characteristic x-ray Bragg profiles. The ergodic state, on the other hand, is not expected to show long-range ferroelectric order after poling and is expected to exhibit a cubiclike (CL) average structure on the global scale even after experiencing strong field. The XRPD patterns of the unpoled specimens were obtained after thermal annealing the ground powder at $\sim 700\,^\circ$C. The patterns of the unpoled specimens for both series (NBT-20KBT-xKNN and NBT-6BT-yKNN) suggest a CL average structure [70], Fig. 2(a). The XRPD patterns

of the poled specimens, on the other hand, suggest distinct ferroelectric structural distortions, Fig. 2(b). Consistent with the previous studies [35,40–42], the diffraction patterns of the poled KNN-free compositions ($x = 0$, $y = 0$) exhibit rhombohedral average structure (the pseudocubic $\{111\}_{pc}$ profile is a doublet, and the $\{200\}_{pc}$ profile is a singlet). The XRD pattern of poled NBT-20KBT-xKNN with $x = 0.01$, on the other hand, shows an additional small hump in the $\{200\}_{pc}$ pseudocubic Bragg profile [shown with arrows in Fig. 2(b)], suggesting a field-stabilized long-range-ordered ferroelectric tetragonal distortion. For $x = 0.015$, the intensity of the tetragonal Bragg peaks increased considerably, while that of the rhombohedral peaks decreased. The peaks corresponding to the long-range rhombohedral ferroelectric distortion become invisible for $x = 0.02$. The XRPD pattern of poled $x = 0.02$ can be explained in terms of the mixture of CL and tetragonal *P4mm* phases, Fig. S3(b) in the Supplemental Material [67]. For $x = 0.03$, the composition exhibiting maximum electrostrain, even the long-range tetragonal *P4mm* is barely visible. A careful observation, however, reveals that a small fraction of the long-range tetragonal ferroelectric order could still be stabilized for this composition, Fig. S4 in the Supplemental Material [67]. For $x \geqslant 0.04$, there is no detectable difference between the XRD patterns of poled and unpoled specimens, Fig. S4 in the Supplemental Material [67]. This composition is therefore in the full ER state. The same sequence of structural evolution can be seen in the NBT-6BT-yKNN series, Fig. 3. For this case, the complete
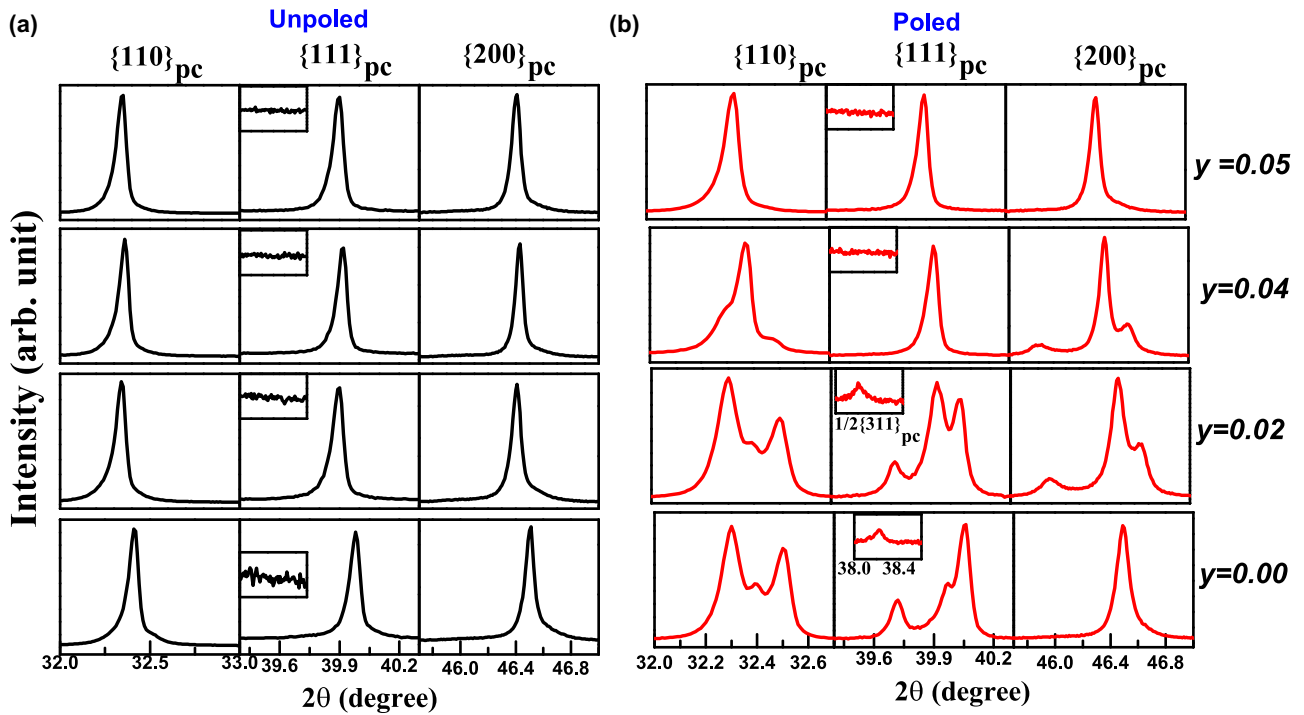
FIG. 3. X-ray powder diffraction Bragg profiles of pseudocubic $\{110\}_{pc}$, $\{111\}_{pc}$, and $\{200\}_{pc}$ of (a) unpoled and (b) poled NBT-6BT-(y)KNN.

ergodic state sets in at a relatively higher KNN concentration, $y = 0.06$ [Fig. 3(b)].

C. Average global structure: Neutron diffraction

Figures 4(a) and 4(b) shows the NPD patterns of selected compositions of unpoled NBT-20KBT-xKNN and NBT-6BT-yKNN. For the sake of clarity, only limited 2θ regions are shown to highlight the superlattice peaks corresponding to in-phase octahedral tilt ($0.5\{ooe\}_{pc}$ pseudocubic indices where o and e represent odd and even integers, respectively) and superlattice peaks corresponding to the antiphase octahedral tilt (with pseudocubic indices $0.5\{ooo\}_{pc}$). The composition $x = 0.00$ shows superlattice peaks with pseudocubic indices $0.5\{310\}_{pc}$ and $0.5\{311\}_{pc}$, suggesting the presence of both $R3c$ and $P4bm$ phases. The intensity of $0.5\{310\}_{pc}$ superlattice reflection grows with the increasing concentration of KNN. This is accompanied by a concomitant decrease in the intensity of the $0.5\{311\}_{pc}$ superlattice peak corresponding to the $R3c$ phase, Fig. 4(a). For $x = 0.03$, the $0.5\{311\}_{pc}$ superlattice peak is no longer visible. The NPD pattern of this (and higher) composition shows superlattice reflections corresponding to the in-phase octahedral tilt, suggesting that the unpoled specimens of these compositions exhibit only $P4bm$ phase on the global scale. The same trend can be seen in the NPD patterns of the unpoled NBT-6BT-yKNN series, Fig. 4(b). On poling the compositions $x < 0.03$, the intensity of the $0.5\{311\}_{pc}$ superlattice peak is significantly enhanced, and the intensity of the $0.5\{310\}_{pc}$ superlattice peak is reduced, Figs. 4(c) and 4(d). This suggests a field-driven irreversible $P4bm$-to-$R3c$ transformation. In contrast, no visible effect on the intensity of the $0.5\{310\}_{pc}$ superlattice peak can be seen for $x \geqslant 0.03$.

D. Average local structure: Eu^{+3} PL

For a better appreciation of the nature of the CL phase, we carried out local structural analysis using Eu^{+3} PL [61–64]. This technique exploits the sensitivity of the Stark bands in the PL emission spectrum on the local environment around the active emitting center (the doped rare-earth cation). In brief, while the f-f electronic transitions in isolated rare-earth elements/ions are parity forbidden, such transitions become possible when the ions are perturbed by the crystal field of the surrounding ligand. The subtler details of a given Stark band in the PL spectrum are sensitive to the strength and symmetry of the crystal field of the ligand/host matrix. This aspect makes it possible to use the doped rare-earth ions in a given host to act as probes to monitor structural changes on the local scale caused by changes in the chemical composition, temperature, and pressure [71–73]. Because of the relative simplicity of interpreting the emission spectra of Eu^{+3} PL, we chose to dope our systems with a dilute concentration of Eu^{+3} as per the nominal formula Na$_{0.5}$Bi$_{0.495}$Eu$_{0.005}$TiO$_3$. Such a small Eu^{+3} concentration is sufficient to give a good PL signal without noticeably affecting the structural and physical properties of the original (undoped) composition [38,62].

The different Stark bands of the Eu^{+3} PL spectrum correspond to the different (J) $^5D_0 \rightarrow \,^7F_J$ radiative electronic transitions: $^5D_0 \rightarrow \,^7F_0$ (570–585 nm), $^5D_0 \rightarrow \,^7F_1$ (585–600 nm), $^5D_0 \rightarrow \,^7F_2$ (610–630 nm), $^5D_0 \rightarrow \,^7F_3$ (640–660 nm), and $^5D_0 \rightarrow \,^7F_4$ (680–710 nm), Fig. S5 in the Supplemental Material [67]. Since the multiplicity of the ^7F_J level increases with increasing J, the Stark band corresponding to a higher J shows overlap of several peaks. To minimize ambiguity in the interpretation of the data, we prefer to use the Stark band corresponding to $J = 0$ (expected to be a
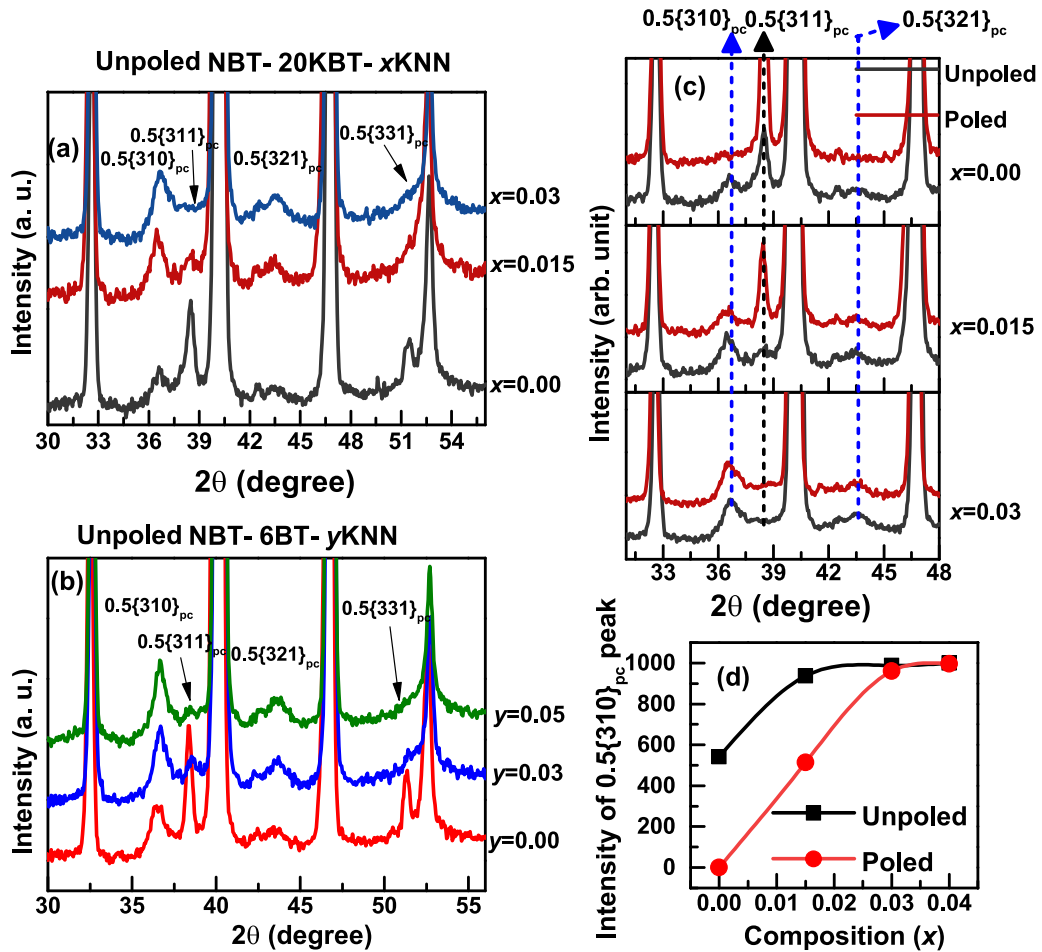
FIG. 4. Neutron powder diffraction (NPD) patterns of select unpoled specimens of (a) NBT-20KBT-xKNN and (b) NBT-6BT-yKNN. The superlattice peaks are shown with half-integer pseudocubic indices. Superlattice peaks of the type $\frac{1}{2}$ {odd odd even}$_{pc}$ correspond to in-phase octahedral tilt, and those with indices $\frac{1}{2}$ {odd odd odd}$_{pc}$ represent antiphase octahedral tilt. (c) Comparison of the NPD patterns of unpoled and poled $x = 0.00, 0.015,$ and 0.03 of NBT-20KBT-xKNN. Note that the electric field completely suppresses superlattice reflections corresponding to the in-phase tilts for $x = 0.00$, but these reflections are unaffected after poling for $x \geqslant 0.03$. (d) Composition dependence of the integrated intensity of the $0.5\{310\}_{pc}$ superlattice peak in the unpoled and poled states of NBT-20KBT-xKNN.

singlet). As shown in Fig. 5(a), the $^7F_0$ Stark band of unpoled $x = 0.00$ is a doublet (peak-1 at ~578.9 nm and peak-2 at ~579.71 nm). Poling suppresses peak-1 and retains peak-2. Given that the average structure of the poled $x = 0.00$ is $R3c$, Fig. 2(b), peak-2 of the $^7F_0$ doublet is representative of the rhombohedral structure [Fig. 5(a)]. Peak-1 is attributed to the $P4mm$ distortion [38,41,62]. Like $x = 0.00$, the $^7F_0$ Stark band of unpoled $x = 0.015$ is also a doublet. However, for this composition, peak-1 is partially suppressed after poling. The extent of suppression of peak-1 after poling is significantly reduced for $x = 0.02$, Fig. 5(c). For $x > 0.02$, poling did not change the shape of the $^7F_0$ Stark profile, Fig. 5(d).

E. Eu^{+3} PL and XRD *in situ* with field

To appreciate the field-driven structural changes on both the local and global scales, we carried out XRD and Eu^{+3} PL studies *in situ* with an electric field on a representative composition $x = 0.03$. It is interesting to note that the shape of the $^7F_0$ Stark profile did not change even while a field of 50 kV/cm was applied, Fig. 6(a). This may seem to

suggest that the structural state of the system is insensitive to the applied field for this composition. We performed field-dependent XRD measurements in reflection geometry using a laboratory x-ray diffractometer. We noted that, in contrast to the diffraction patterns obtained from an unpoled powder specimen of the same composition, diffraction patterns obtained from the unpoled pellets show additional broad humps [marked with arrows in Fig. 6(b)] on the left of both $\{111\}_{pc}$ and $\{200\}_{pc}$ CL Bragg profiles. To ascertain the origin of these additional peaks, we carried out diffraction measurements in transmission geometry using high-energy synchrotron x rays (wavelength 0.207308 Å). It is evident from Fig. S6(b) in the Supplemental Material [67] that the diffraction pattern obtained in transmission geometry from the unpoled disc mimics the diffraction pattern of the powder specimen. Since the synchrotron x-ray beam (~1 × 1 mm cross-section) passes through a ~0.7-mm-thick disc, the synchrotron XRD pattern is averaged over the entire volume of the pellet specimen. The penetration depth of the Cu $K\alpha$ (the laboratory x-ray source), on the other hand, is only a few microns beneath the surface. This experiment confirms that the additional reflections seen
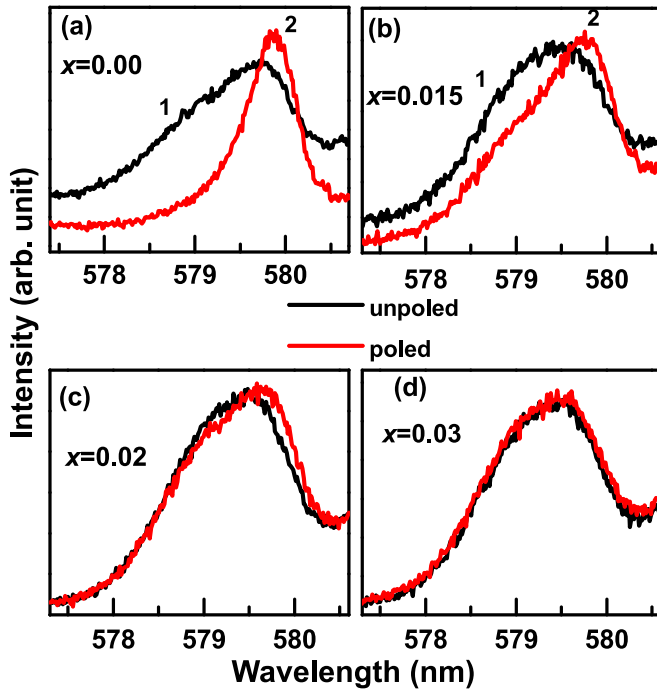
FIG. 5. (a)–(d) $^5D_0 \rightarrow {}^7F_0$ (570–585 nm) Stark profiles of the Eu^{+3} photoluminescence spectra obtained from unpoled and poled specimens of Eu-doped NBT-20KBT-xKNN. The $^7F_0$ Stark band of unpoled $x = 0.00$ is a doublet (peak-1 at ∼578.9 nm and peak-2 at ∼579.71 nm are the fingerprints of $P4mm$ and $R3c$ phases, respectively).

in the laboratory XRD patterns of the pellets are from the grains near the surface region of the pellets. Such differences in the diffraction patterns from surface and bulk regions have also been reported for NBT-based system [74,75]. For the sake of consistency with the field-dependent Eu^{+3} PL measurements (the Eu^{+3} PL signals are also from the surface grains), we performed XRD measurements *in situ* with an electric field in reflection geometry using the laboratory XRD. In contrast to the field-dependent Eu^{+3} PL measurements which show no effect of the electric field on the PL spectrum, we found dramatic changes in the shapes of the x-ray Bragg profiles on the application of the electric field, Fig. 6(b). Both $\{111\}_{pc}$ and $\{200\}_{pc}$ profiles developed considerable asymmetry when a field of 50 kV/cm was applied [Fig. 6(b)]. This suggests a field-driven CL $\rightarrow R3c + P4mm$ transformation. On switching off the field, the asymmetry in both $\{111\}_{pc}$ and $\{200\}_{pc}$ profiles reduced considerably. A careful observation, however, reveals some remanence of the long-range tetragonal order (Fig. S6(a) in the Supplemental Material [67]). This is consistent with the fact that d_{33} of this composition is still ∼105 pC N [Fig. 1(a)], and the depolarization temperature is above room temperature (∼60 °C). Since the Eu^{+3} PL of unpoled $x = 0.03$ confirms the coexistence of $R3c$ and $P4mm$ distortions on the local scale [Fig. 5(d)], the absence of a noticeable change in the relative intensities of peak-1 and peak-2 of the $^7F_0$ Stark profile even when a field 50 kV/cm is applied can be rationalized by arguing that the electric field does not alter the relative fractions of the $P4mm$ and $R3c$ distortions. In view of this, the CL $\rightarrow R3c + P4mm$ transformation on

the global scale is merely a manifestation of the increase in the correlation lengths of the short-range rhombohedral and tetragonal regions without noticeably altering their relative volume fractions.

F. Lattice strain and macroscopic electrostrain

Having shown above that the compositions showing large electrostrain are those exhibiting field-driven transformation of the short-ranged $R3c$ and $P4mm$ domains to long-ranged $R3c$ and $P4mm$ domains, we sought a correspondence between the degree of reversibility of these structural processes with the unipolar electrostrain measured across the different compositions of the NBT-20KBT-xKNN series. Because of the severe overlap of the Bragg profiles corresponding to the tetragonal, rhombohedral, and CL phases, we did not attempt to deconvolute the individual Bragg profiles and calculate their integrated intensities for estimating the domain switching fraction [76]. We instead sought to estimate the degree of reversibility of the multiple interlinked structural processes occurring simultaneously by monitoring the relative shift in the peak position of the CL Bragg profile 200_{CL}, Figs. 6(b), S7, and S8 in the Supplemental Material [67]. Accordingly, we calculated the strain ε_{200}^{CL} developed in the 200_{CL} plane as a function of the applied field for the different compositions of NBT-20KBT-xKNN, Figs. 7(a)–7(f). The remanent ε_{200}^{CL} is maximum for the KNN-free composition ($x = 0$). It decreases systematically with increasing x and is zero for $x = 0.04$, the composition in the fully ER state. It is important to note that the reversible lattice strain, defined as the difference between ε_{200}^{CL} (max) and ε_{200}^{CL} (remanent), exhibits a maximum at $x = 0.03$, the composition which exhibits the maximum macroscopic electrostrain/d_{33}^* in this series, Fig. 7(g).

G. Field-driven ferroelectric-to-relaxor transition and *E-x* phase diagram

In Sec. III A, we highlighted that the remanent polarization drops abruptly at $x = 0.02$ and 0.04 [Figs. 1(e) and 1(g)] for the NBT-20KBT-xKNN series and at $y = 0.04$ and 0.06 for the NBT-6BT-yKNN series [Figs. 1(f) and 1(h)]. A careful observation reveals that these abrupt drops are manifestations of a qualitative change in the shape of the bipolar P-E curves. This is more clearly revealed in the bipolar switching current (I) vs field (E) measurements, Figs. 8(a)–8(c) and S9(a)–S9(f) in the Supplemental Material [67]). While the compositions $x < 0.02$ exhibit two current peaks at E_{F1} and E_{F2}, typical of domain switching events in normal ferroelectrics during bipolar cycling [Figs. 8(b) and 8(c)], the compositions $x = 0.02$ and 0.03 exhibit four current peaks (two current peaks in the positive cycle and two in the negative cycle) during bipolar cycling. For $x \geqslant 0.04$, the current peaks are significantly broadened. To appreciate the significance of the two current peaks in the positive cycle and two in the negative cycle, we carried out XRD (in reflection geometry) *in situ* with the electric field by applying the field in the positive and negative directions on the representative composition $x = 0.03$. The experiment involved collecting diffraction patterns on a virgin circular disc and subsequently after poling the disc with a field of 50 kV/cm. The difference in the XRD pattern of the poled and unpoled represents the irreversible changes induced by
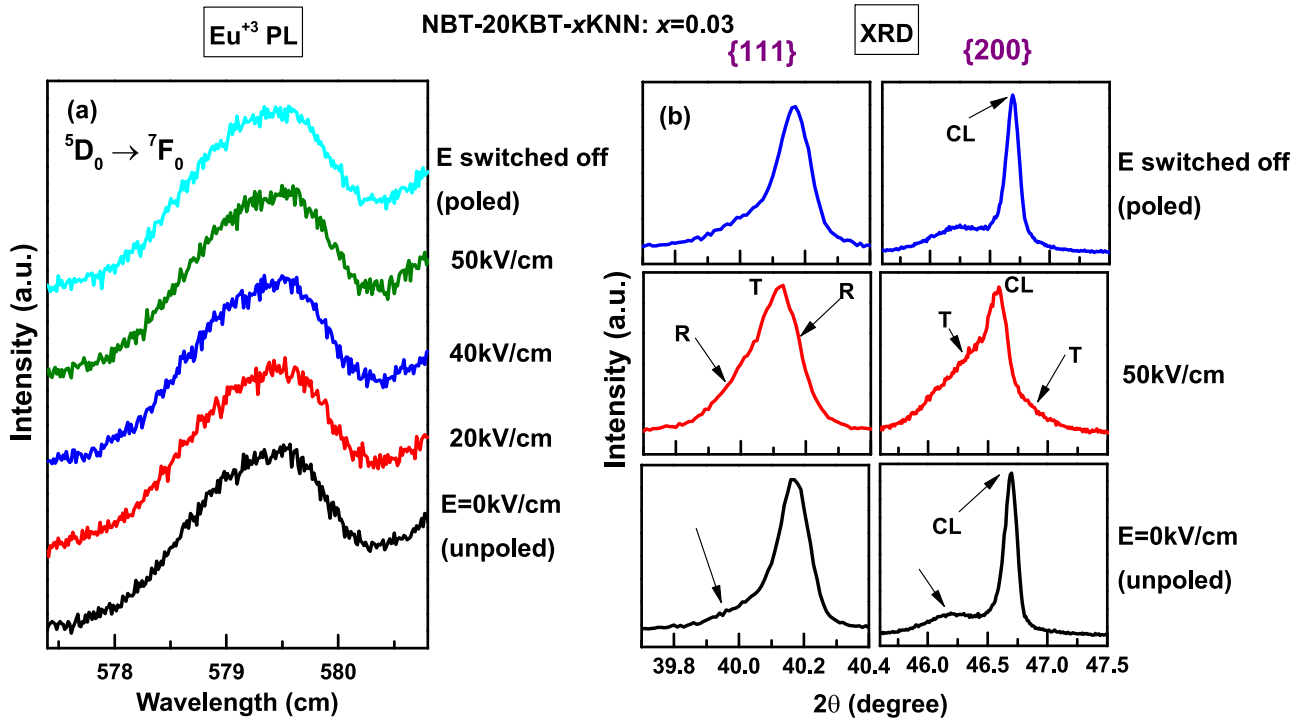
FIG. 6. (a) Evolution of the $^5D_0 \rightarrow {}^7F_0$ Stark profiles of Eu-doped NBT-20KBT-(x)KNN: $x = 0.03$ as a function of unipolar electric field. (b) Evolution of the x-ray diffraction (XRD) Bragg profiles of $\{111\}_{pc}$ and $\{200\}_{pc}$ pseudocubic reflections in the unpoled, at 50 kV/cm, and after switching off the field. The arrows in (b) indicate peak positions of different phases where R, CL, and T are rhombohedral ($R3c$), cubiclike, and tetragonal $P4mm$ phases, respectively.

the poling field. When the field direction was reversed and gradually increased (in the negative direction), we found that there exists a critical field at which the diffraction pattern exactly matched the diffraction pattern of the unpoled state. On increasing the field further in the negative direction, the difference in the diffraction pattern with respect to the unpoled state increases again. This interesting behavior is quantitatively shown in Fig. 9(d) in terms of the field dependence of ε_{200}^{CL} during bipolar cycling of the different compositions of the NBT-20KBT-xKNN series. It is evident that, for compositions in the fully nonergodic state, it is not possible to return to $\varepsilon_{200}^{CL} = 0$ during the field reversal. For $x = 0.03$, a composition exhibiting a nonergodic + ergodic mixed state, $\varepsilon_{200}^{CL} = 0$ at -16 kV/cm. This is true for all compositions exhibiting mixed (ergodic + nonergodic) state $0.02 \leqslant x \leqslant 0.03$. In view of these observations, the current peak labeled E_{R1} in the negative cycle of Fig. 8(d) is attributed to the field-driven ferroelectric–to–NER + ER transformation. The second peak E_{F2} at higher field is attributed to the switching of the ferroelectric domains. Correspondingly, the current peak at E_{R2} in the positive cycle is attributed to the field-driven ferroelectric–to–NER + ER, and the peak at E_{F1} is attributed to the switching of the ferroelectric domains. We used this structural understanding of the bipolar *I-E* plots to draw an *E-x* phase diagram, Fig. 8(d). This phase diagram shows the variation of the polar states (with respect to the polar states of the poled specimen) when the field is applied in the opposite direction. The diagram clearly shows three distinct compositional ranges: (i) ferroelectric for the compositions ($x = 0.00-0.015$), (ii) a mixture of ER and ferroelectric states

for $0.015 < x < 0.04$, and (iii) the ER state for $x \geqslant 0.04$. Based on our field-driven Eu^{+3} PL and XRD studies, the ergodic state is designated as a mixture of $R3c$ and $P4mm$ short-range orders. We show the corresponding *E-y* phase diagram of the NBT-6BT-yKNN system in Fig. S9(g) in the Supplemental Material [67].

IV. DISCUSSION

In this paper, we clearly show that KNN modification introduces two important structural features: (i) ferroelectric tetragonal distortion and (ii) increased propensity for in-phase octahedral tilt in both 0.94NBT-6BT-yKNN and 0.80NBT-0.20KBT-xKNN. While the onset of the long-range tetragonal phase creates coexistence of ferroelectric phases ($P4mm$ and $R3c$) and improves the weak-signal piezoelectric response (the best d_{33} is obtained for $x = 0.015$ for NBT-KBT-xKNN and $y = 0.02$ for NBT-BT-KNN), the increased propensity of the in-phase octahedral tilt completely alters the ferroelectric switching behavior and enhances the electromechanical response. As the in-phase octahedral tilt is not compatible with the long-range $P4mm$ and $R3c$ ferroelectric orders, it increasingly destabilizes them. The long-range rhombohedral ferroelectric order ceases at $x = 0.025$, while the tetragonal long-range order persists to some extent until $x = 0.03$. For $x \geqslant 0.04$, even the long-range tetragonal ferroelectric order vanishes, and the system is completely in the ER state. The mixed (coexistence of nonergodic and ergodic) state lies in the composition range $0.02 \leqslant x < 0.04$ and is most neatly and convincingly characterized by two
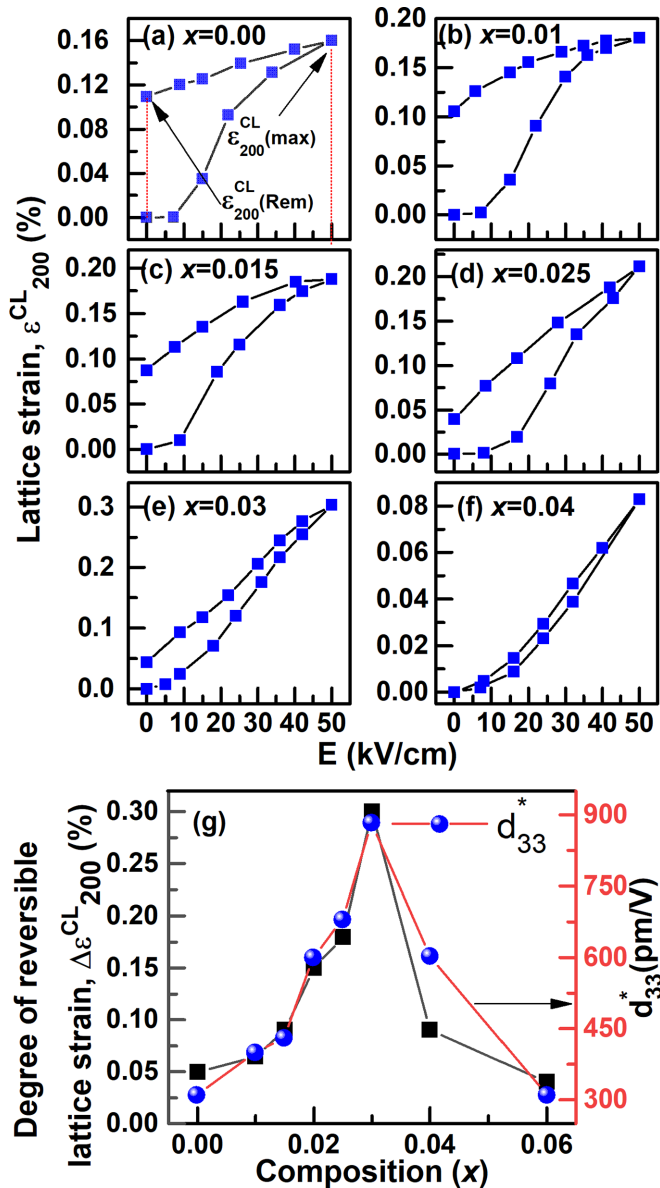
FIG. 7. (a)–(f) Field dependence of the 200_{CL} lattice strain of different compositions of NBT-20KBT-xKNN during increasing and decreasing field. The measurement was done on an unpoled specimen. ε_{200}^{CL}(max) and ε_{200}^{CL}(Rem) indicate maximum lattice strain and remanent lattice strain, respectively. (g) Composition dependence of the reversible 200 strain, $\Delta\varepsilon^R$ [$=\varepsilon_{200}^{CL}$(max) $- \varepsilon_{200}^{CL}$(Rem)] and large field effective converse piezoelectric coefficient d_{33}^*. Note the one-to-one correspondence between $\Delta\varepsilon^{CL}$ and d_{33}^*.

positive current peaks in the positive cycle and two negative current peaks in the negative cycle of the bipolar field switching measurements, Fig. 8(d). The two peaks in the positive cycle correspond to ferroelectric ($\downarrow$)-to-relaxor and then relaxor-to-ferroelectric ($\uparrow$) transformations, respectively. This phenomenon was highlighted by Guo et al. [77] in [(Na$_{1/2}$Bi$_{1/2}$)$_{0.95}$Ba$_{0.05}$]$_{0.98}$La$_{0.02}$TiO$_3$, wherein the relaxor state was attributed to the $P4bm$ phase and the ferroelectric state to the $R3c$ phase. Our combination of Eu$^+$ PL and XRD studies *in situ* with the electric field have, on the other hand, revealed that the ER + NER states in

NBT-20KBT-KNN are a mixture of $R3c$ and $P4mm$ distortions on a smaller length scale. For compositions exhibiting a mixed (ergodic + nonergodic) state, the electric field merely increases the correlation length of these ferroelectric distortions simultaneously without changing the overall volume fractions of the $P4mm$ and $R3c$ distortions. Our observation is consistent with Kling et al. [58] on 0.91NBT-0.06BT-0.03KNN, who reported that, although the electric field significantly changed the domain morphology, the diffraction patterns remained unchanged. Hinterstein et al. [59] investigated a composition with slightly lower KNN concentration (0.92NBT-0.06BT-0.02KNN) and reported a field-driven $a^0a^0c^+$-to-$a^-a^-a^-$ tilt transition. A similar field-driven $P4bm$-to-$R3c$ transformation has also been reported by Liu and Tan [78] in their transmission electron microscopy study of [(Na$_{0.84}$K$_{0.16}$)$_{0.5}$Bi$_{0.5}$]$_{0.96}$Sr$_{0.04}$(Ti$_{0.975}$Nb$_{0.025}$)O$_3$. However, in all these studies, the ferroelectric phase has been identified with the $R3c$ distortion, and the tetragonal phase is attributed to the $P4bm$ distortion comprising $a^0a^0c^+$ octahedral tilt. If the tetragonal phase in the system were only to be attributed to the $P4bm$ structure, then the splitting of the CL $\{200\}_{pc}$ Bragg profile on the application of an electric field (Figs. 6(b) and S7(b) in the Supplemental Material [67]) would imply that the electric field promotes the $P4bm$ phase along with the $R3c$ phase. However, this interpretation would be inconsistent with the fact that the $\frac{1}{2}\{ooe\}$ superlattice reflections, characteristic of the $P4bm$ phase, weaken with increasing field [58]. The signature of the tetragonal distortion seen in the XRD measurements *in situ* with the electric field (Figs. 6(b) and Fig. S7(b) in the Supplemental Material [67]) is therefore characteristic of the development of the long-range tetragonal $P4mm$ ferroelectric phase. Levin et al. [37] and, more recently, Adhikary et al. [41] have shown that the ferroelectric $P4mm$ and the $a^0a^0c^+$ tilt distortions are not coupled in NBT-based solid solutions, as they appear at different temperatures on cooling from the cubic phase; the in-phase tilt sets in well above the temperature corresponding to the onset of the ferroelectric $P4mm$ distortion [38,41,79].

It is worth highlighting that, while the onset of tetragonal $P4mm$ distortion in KNN-free NBT-BT and NBT-KBT increases the depolarization temperature [42,43,79], the depolarization temperature of NBT-20KBT-KNN continues to decrease even while the $P4mm$ distortion sets in (Fig. S2(c) in the Supplemental Material [67]). For example, the depolarization temperature of NBT-6BT (which stabilizes only the $R3c$ phase in the poled specimen) is 100 °C. It increases to 140 °C for NBT-0.07BT, a composition that shows long-range tetragonal ferroelectric distortion [80]. In contrast, although KNN also induces a long-range $P4mm$ ferroelectric distortion, it fails to increase the depolarization temperature in both NBT-20KBT-xKNN and NBT-6BT-yKNN series, Fig. S2(c) in the Supplemental Material [67]. The continuous decrease in T_d in the KNN-modified compositions can be rationalized from two factors: (i) the tetragonality ($c/a-1$) of the $P4mm$ distortion in the KNN-modified NBT-0.20KBT-1.5KNN is 1.15%, Fig. S10 in the Supplemental Material [67]. This value is notably smaller than the tetragonality of 1.4% in the KNN-free tetragonal composition 0.75NBT-0.25KBT [79]. (ii) KNN also furthers the propensity for the in-phase octahedral tilt [Fig. 4(a)], which helps in suppressing the long-range ferro-
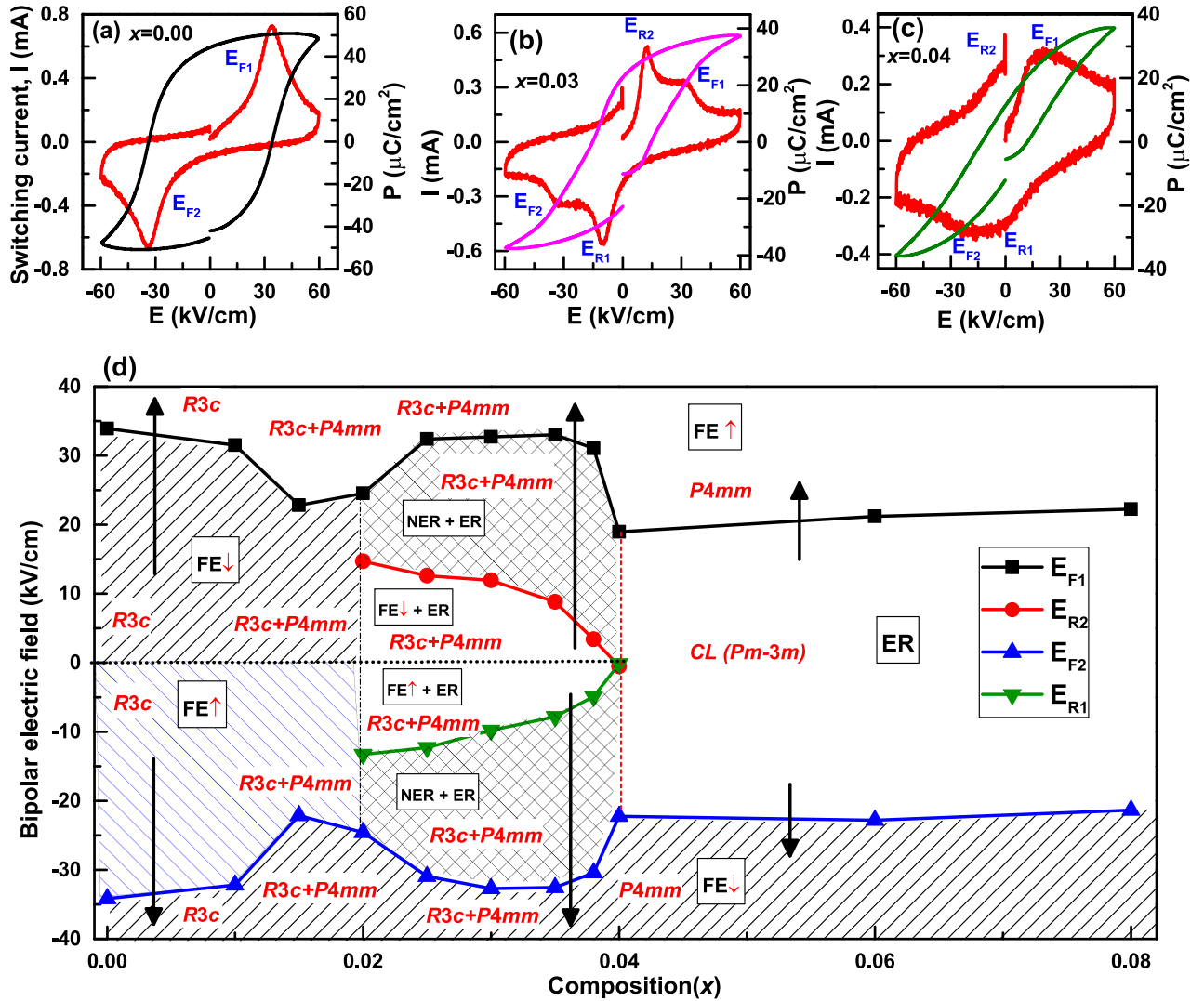
FIG. 8. Field dependence of the switching current (*I*) and *P-E* loops of NBT-20KBT-*x*KNN (a) $x = 0.00$, (b) $x = 0.03$, and (c) $x = 0.04$. (d) Electric field composition phase diagram derived from the switching current and field-dependent x-ray diffraction (XRD) measurements. In this diagram, up to $x = 0.04$, the zero-field state corresponds to the poled state with polarization ↓ or ↑. For $x \leqslant 0.02$, the field stabilized long-range ferroelectric order is preserved, and changing the direction of the field merely changes the orientation of the polarization. In the composition range $0.02 < x < 0.04$, the system exhibits field-driven ferroelectric–to–nonergodic relaxor (NER) + ergodic (ER) transformation at lower fields and NER + ER–to–ferroelectric transformation at higher fields. Black and red arrows indicate the direction of electric field and the orientation of polarization, respectively.

electric order and promotes the onset of the ergodic state. In contrast, despite the persistence of the in-phase tilted octahedral regions, the ergodic state does not exist in the KNN-free compositions of both series.

V. CONCLUSIONS

In summary, our detailed scrutiny of the KNN-modified MPB compositions of NBT-based lead-free piezoelectrics (NBT-KBT and NBT-BT) as a function of composition and electric field revealed fresh structural insights regarding the microscopic mechanisms governing the electric-field-driven strain and polarization switching behavior of these systems. We show that KNN modification brings in two important structural distortions: (i) the ferroelectric tetragonal (*P4mm*)

phase and (ii) increased propensity for in-phase octahedral tilt. While the *P4mm* distortion takes the system in a two-phase ferroelectric state and notably improves the weak-field piezoelectric response, the increased propensity for the in-phase octahedral tilt gradually overwhelms the system and promotes an ER state comprising short-range *R3c* and *P4mm* ferroelectric regions. In contrast to the common perception, we show that the highest electrostrain is achieved when the system is in the mixed (ergodic + nonergodic) state, wherein the electric field increases the correlation lengths of the short-ranged *R3c* and *P4mm* regions without inducing any noticeable inter-ferroelectric transformation. We also show that the onset of the ER state dramatically changes the polarization switching behavior, and the system exhibits a relatively less-known phenomenon of long-range ferroelectric order transforming to a
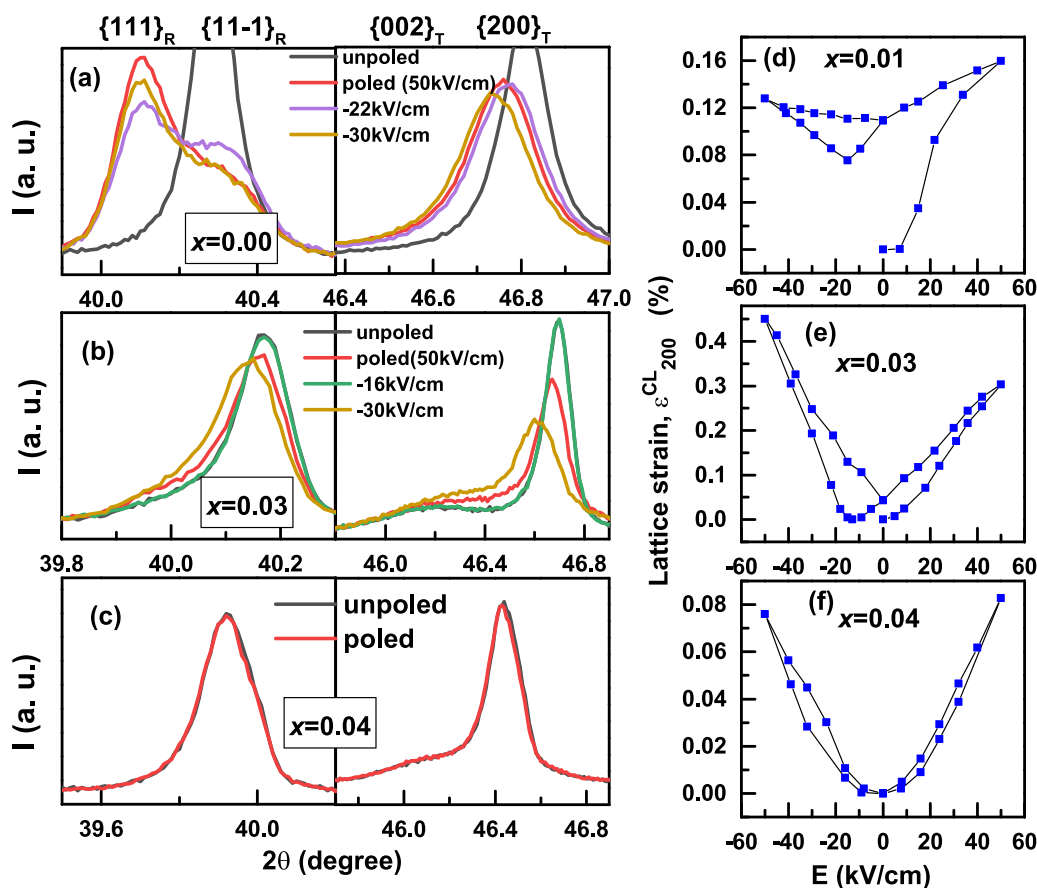
FIG. 9. X-ray diffraction (XRD) Bragg profiles of unpoled, positively poled, and during application of field in the negative direction on NBT-20KBT-xKNN with (a) $x = 0.00$ and (b) $x = 0.03$. (c) XRD patterns of unpoled and poled $x = 0.04$. Note that, in (b), the diffraction pattern of the unpoled state can be exactly reproduced after application of a critical field (-13 kV/cm) in the negative direction. (d)–(f) Variation of the 200 lattice strain under bipolar cycling of $x = 0.00$, 0.03, and 0.04.

NER state during field reversal during bipolar cycling. We summarize these findings in the form of a comprehensive electric field composition phase diagram of both systems. Though this paper is focused on KNN-modified MPB compositions of NBT-KBT and NBT-BT, the general features highlighted here are likely to be true for other NBT-based MPB systems.

ACKNOWLEDGMENTS

[1] E.U. Directive 2002/95/EC: Restriction of the use of certain hazardous substances in electrical and electronic equipment (RoHS), Off. J. Eur. Communities **46**, 19 (2003).

[2] Y. Saito, H. Takao, T. Tani, T. Nonoyama, K. Takatori, T. Homma, T. Nagaya, and M. Nakamura, Nature (London) **432**, 84 (2004).

[3] J. Rödel, W. Jo, K. T. P. Seifert, E.-M. Anton, T. Granzow, and D. Damjanovic, J. Am. Ceram. Soc. **92**, 1153 (2009).

[4] J. Rödel and J.-F. Li, MRS Bull. **43**, 576 (2018).

[5] T. Zheng, J. Wu, D. Xiao, and J. Zhu, Prog. Mater. Sci. **98**, 552 (2018).

[6] C. L. Zhao, H. J. Wu, F. Li, Y. Cai, Y. Zhang, D. Song, J. G. Wu, X. Lyu, J. Yin, D. Q. Xiao *et al.*, J. Am. Chem. Soc. **140**, 15252 (2018).

[7] R. Ranjan, Curr. Sci. **118**, 1507 (2020).

[8] J. Wu, J. Appl. Phys. **127**, 190901 (2020).

[9] W. Liu and X. Ren, Phys. Rev. Lett. **103**, 257602 (2009).

[10] J. Gao, X. Ke, M. Acosta, J. Glaum, and X. Ren, MRS Bull. **43**, 595 (2018).

[11] D. S. Keeble, F. Benabdallah, P. A. Thomas, M. Maglione, and J. Kreisel, Appl. Phys. Lett. **102**, 092903 (2013).

[12] D. Damjanovic, A. Biancoli, L. Batooli, A. Vahabzadeh, and J. Trodahl, Appl. Phys. Lett. **100**, 192907 (2012).

[13] M. Acosta, N. Khakpash, T. Someya, N. Novak, W. Jo, H. Nagata, G. A. Rossetti, Jr., and J. Rodel, Phys. Rev. B **91**, 104108 (2015).

[14] K. Brajesh, K. Tanwar, M. Abebe, and R. Ranjan, Phys. Rev. B **92**, 224112 (2015).

[15] K. Brajesh, M. Abebe, and R. Ranjan, Phys. Rev. B **94**, 104108 (2016).

[16] M. Abebe, K. Brajesh, A. Mishra, A. Senyshyn, and R. Ranjan, Phys. Rev. B **96**, 014113 (2017).

[17] T. Iamsasri, G. Tutuncu, C. Uthaisar, S. Wongsaenmai, S. Pojprapai, and J. L. Jones, J. Appl. Phys. **117**, 024101 (2015).

[18] K. Xu, J. Li, X. Lv, J. G. Wu, X. X. Zhang, D. Q. Xiao, and J. G. Zhu, Adv. Mater. **28**, 8519 (2016).

[19] B. Wu, H. J. Wu, J. G. Wu, D. Q. Xiao, J. G. Zhu, and S. J. Pennycook, J. Am. Chem. Soc. **138**, 15459 (2016).

[20] A. R. Paterson, H. Nagata, X. Tan, J. E. Daniels, M. Hinterstein, R. Ranjan, P. B. Groszewicz, W. Jo, and J. L. Jones, MRS Bull. **43**, 600 (2018).

[21] S.-T. Zhang, A. B. Kounga, E. Aulbach, H. Ehrenberg, and J. Rödel, Appl. Phys. Lett. **91**, 112906 (2007).

[22] I. G. Siny, C.-S. Tu, and V. H. Schmidt, Phys. Rev. B **51**, 5659 (1995).

[23] V. V. Shvartsman and D. C. Lupascu, J. Am. Ceram. Soc. **95**, 1 (2012).

[24] Y. Hiruma, H. Nagata, and T. Takenaka, J. Appl. Phys. **105**, 084112 (2009).

[25] G. A. Smolenskii, V. A. Isupv, A. I. Afranovskaya, and N. N. Kainik, J. Solid State Phys. **11**, 2651 (1961).

[26] J. Kreisel, P. Bouvier, B. Dkhil, P. A. Thomas, A. M. Glazer, T. R. Welberry, B. Chaabane, and M. Mezouar, Phys. Rev. B **68**, 014113 (2003).

[27] V. Dorcet and G. Trolliard, Acta Mater. **56**, 1753 (2008).

[28] G. O. Jones and P. A. Thomas, Acta Cryst. B **58**, 168 (2002).

[29] I. Levin and I. M. Reaney, Adv. Funct. Mater. **22**, 3445 (2012).

[30] E. Aksel, J. S. Forrester, J. L. Jones, P. A. Thomas, K. Page, and M. R. Suchomel, Appl. Phys. Lett. **98**, 152901 (2011).

[31] S. Gorfman and P. A. Thomas, J. Appl. Cryst. **43**, 1409 (2010).

[32] A. M. Balagurov, E. Y. Koroleva, A. A. Naberezhnov, V. P. Sakhnenko, B. N. Savenko, N. V. Ter-Oganessian, and S. B. Vakhrushev, Phase Transit. **79**, 163 (2006).

[33] B. N. Rao, R. Datta, S. S. Chandrashekaran, D. K. Mishra, V. Sathe, A. Senyshyn, and R. Ranjan, Phys. Rev. B **88**, 224103 (2013).

[34] B. N. Rao and R. Ranjan, Phys. Rev. B **86**, 134103 (2012).

[35] R. Garg, B. N. Rao, A. Senyshyn, P. S. R. Krishna, and R. Ranjan, Phys. Rev. B **88**, 014103 (2013).

[36] A. Sasaki, T. Chiba, Y. Mamiyal, and E. Otsuki, Jpn. J. Appl. Phys. **38**, 5564 (1999).

[37] I. Levin, I. M. Reaney, E.-M. Anton, W. Jo, J. Rödel, J. Pokorny, L. A. Schmitt, H.-J. Kleebe, M. Hinterstein, and J. L. Jones, Phys. Rev. B **87**, 024113 (2013).

[38] G. D. Adhikary, D. K. Khatua, A. Senyshyn, and R. Ranjan, Acta Mater. **164**, 749 (2019).

[39] T. Takenaka, K. Maruyama, and K. Sakata, Jpn. J. Appl. Phys. **30**, 2236 (1991).

[40] C. Ma, H. Guo, and X. Tan, Adv. Funct. Mater. **23**, 5261 (2013).

[41] G. D. Adhikary, D. Sharma, P. Punetha, G. Jafo, G. Abebe, A. Mishra, A. Senyshyn, and R. Ranjan, Phys. Rev. B **104**, 184102 (2021).

[42] G. D. Adhikary, D. K. Khatua, A. Senyshyn, and R. Ranjan, Phys. Rev. B **99**, 174112 (2019).

[43] G. D. Adhikary, D. K. Khatua, A. Mishra, A. De, N. Kumar, S. Saha, U. Shankar, A. Senyshyn, B. N. Rao, and R. Ranjan, Phys. Rev. B **100**, 134111 (2019).

[44] C. Ye, J. Hao, B. Shen, and J. Zhai, J. Am. Ceram. Soc. **95**, 3577 (2012).

[45] J. Hao, B. Shen, J. Zhai, C. Liu, X. Li, and X. Gao, J. Appl. Phys. **113**, 114106 (2013).

[46] K. T. P. Seifert, W. Jo, and J. Rodel, J. Am. Ceram. Soc. **93**, 1392 (2010).

[47] A. Singh and R. Chaterjee, J. Appl. Phys. **109**, 024105 (2011).

[48] W. Bai, L. Li, W. Li, B. Shen, J. Zhai, and H. Chen, J. Alloys Compd. **603**, 149 (2014).

[49] J. Chen, Y. Wang, Y. Zhang, Y. Yang, and R. Jin, J. Eur. Ceram. Soc. **37**, 2365 (2017).

[50] W. Bai, D. Chen, Y. Huang, B. Shen, J. Zhai, and Z. Ji, J. Alloys Compd. **667**, 6 (2016).

[51] S. T. Zhang, A. B. Kounga, E. Aulbach, W. Jo, T. Granzow, H. Ehrenberg, and J. Rödel, J. Appl. Phys. **103**, 034108 (2008).

[52] W. Jo, T. Granzow, E. Aulbach, J. Rödel, and D. Damjanovic, J. Appl. Phys. **105**, 094102 (2009).

[53] W. Jo, R. Dittmer, M. Acosta, J. Zang, C. Groh, E. Sapper, K. Wang, and J. Rödel, J. Electroceram. **29**, 71 (2012).

[54] S. Teranishi, M. Suzuki, Y. Noguchi, M. Miyayama, C. Moriyoshi, Y. Kuroiwa, K. Tawa, and S. Mori, Appl. Phys. Lett. **92**, 182905 (2008).

[55] D. Schutz, M. Deluca, W. Krauss, A. Feteira, T. Jackson, and K. Reichmann, Adv. Funct. Mater. **22**, 2285 (2012).

[56] G. Dong, H. Fan, J. Shi, and M. Li, J. Am. Ceram. Soc. **98**, 1150 (2015).

[57] J. Hao, B. Shen, J. Zhai, C. Liu, X. Li, and X. Gao, J. Am. Ceram. Soc. **96**, 3133 (2013).

[58] J. Kling, X. Tan, W. Jo, H.-J. Kleebe, H. Fuess, and J. Rödel, J. Am. Ceram. Soc. **93**, 2452 (2010).

[59] M. Hinterstein, M. Knapp, M. Hölzel, W. Jo, A. Cervellino, and H. Ehrenberg, J. Appl. Cryst. **43**, 1314 (2010).

[60] W. Jo, J. E. Daniels, J. L. Jones, X. Tan, P. A. Thomas, D. Damjanovic, and J. Rödel, J. Appl. Phys. **109**, 014110 (2011).

[61] D. K. Khatua, A. Kalaskar, and R. Ranjan, Phys. Rev. Lett. **116**, 117601 (2016).

[62] D. K. Khatua, A. Agarwal, N. Kumar, and R. Ranjan, Acta Mater. **145**, 429 (2018).

[63] A. De and R. Ranjan, Phys. Rev. B **98**, 094111 (2018).

[64] A. De and R. Ranjan, J. Appl. Phys. **128**, 124104 (2020).

[65] M. Hoelzel, A. Senyshyn, R. Gilles, H. Boysen, and H. Fuess, Neutron News **18**, 23 (2007).

[66] J. Rodrigues-Carvajal, FULLPROF: A program for Rietveld refinement and pattern matching analysis, Abstracts of the Satellite Meeting on Powder Diffraction of the XV Congress of the IUCr (Toulouse, 1990).

[67] See Supplemental Material at http://link.aps.org/supplemental/10.1103/PhysRevB.107.134108 for pyroelectric current measurements and XRD measurements in situ with an electric field.

[68] L. K. V., A. K. Kalyani, and R. Ranjan, Phys. Rev. B **90**, 224107 (2014).

[69] B. N. Rao, A. N. Fitch, and R. Ranjan, Phys. Rev. B **87**, 060102(R) (2013).

[70] R. Ranjan and A. Dviwedi, Solid State Commun. **135**, 394 (2005).

[71] E. Moret, F. Nicolo, J.-C. G. Bunzli, and G. Chapius, J. Less Common Met. **171**, 273 (1991).

[72] G. Chen, R. G. Haire, J. R. Peterson, and M. M. Abraham, J. Phys. Chem. Solids **55**, 313 (1994).

[73] V. Lavin, T. Troster, U. R. Rodriguez-Mendoza, I. R. Martin, and V. D. Rodriguez, High. Press. Res. **22**, 111 (2002).

[74] S. Kong, N. Kumar, S. Checchia, C. Cazorla, and J. Daniels, Adv. Funct. Mater. **29**, 1900344 (2019).

[75] D. U. Seifert, L. Li, K.-Y. Lee, M. J. Hoffmann, D. C. Sinclair, and M. Hinterstein, J. Eur. Ceram. Soc. **41**, 1221 (2021).

[76] A. Pramanick, D. Damjanovic, J. E. Daniels, J. C. Nino, and J. L. Jones, J. Am. Ceram. Soc. **94**, 293 (2011).

[77] H. Z. Guo, X. M. Liu, F. Xue, L. Q. Chen, W. Hong, and X. L. Tan, Phys. Rev. B **93**, 174114 (2016).

[78] X. Liu and X. Tan, Adv. Mater. **28**, 574 (2016).

[79] G. D. Adhikary, B. Mahale, B. N. Rao, A. Senyshyn, and R. Ranjan, Phys. Rev. B **103**, 184106 (2021).

[80] J. E. Daniels, W. Jo, J. Rödel, and J. L. Jones, Appl. Phys. Lett. **95**, 032904 (2009).